Quasi-universal Behavior of the Threshold Mass in Unequal-mass, Spinning Binary Neutron Star Mergers

Samuel D. Tootle[1] , L. Jens Papenfort[1] , Elias R. Most[2,3,4] , and Luciano Rezzolla[1,5,6]

[1] Institut für Theoretische Physik, Goethe Universität, Max-von-Laue-Str. 1, D-60438 Frankfurt am Main, Germany; tootle@itp.uni-frankfurt.de
[2] Princeton Center for Theoretical Science, Princeton University, Princeton, NJ 08544, USA
[3] Princeton Gravity Initiative, Princeton University, Princeton, NJ 08544, USA
[4] School of Natural Sciences, Institute for Advanced Study, Princeton, NJ 08540, USA
[5] School of Mathematics, Trinity College, Dublin 2, Ireland
[6] Frankfurt Institute for Advanced Studies, Ruth-Moufang-Str. 1, D-60438 Frankfurt am Main, Germany

Abstract

The lifetime of the remnant produced by the merger of two neutron stars can provide a wealth of information on the equation of state of nuclear matter and on the processes leading to the electromagnetic counterpart. Hence, it is essential to determine when this lifetime is the shortest, corresponding to when the remnant has a mass equal to the threshold mass, M_{th}, to prompt collapse to a black hole. We report on the results of more than 360 simulations of merging neutron-star binaries covering 40 different configurations differing in mass ratio and spin of the primary. Using this data, we have derived a quasi-universal relation for M_{th} and expressed its dependence on the mass ratio and spin of the binary. The new expression recovers the results of Koeppel et al. for equal-mass, irrotational binaries and reveals that M_{th} can increase (decrease) by 5% (10%) for binaries that have spins aligned (antialigned) with the orbital angular momentum and provides evidence for a nonmonotonic dependence of M_{th} on the mass asymmetry in the system. Finally, we extend to unequal masses and spinning binaries the lower limits that can be set on the stellar radii once a neutron star binary is detected, illustrating how the merger of an unequal-mass, rapidly spinning binary can significantly constrain the allowed values of the stellar radii.

Unified Astronomy Thesaurus concepts: Compact binary stars (283); General relativity (641); Gravitational collapse (662); Neutron stars (1108); Compact objects (288); Stellar remnants (1627); Black holes (162); Binary pulsars (153)

1. Introduction

With the birth of multimessenger gravitational-wave astronomy and the detection of binary neutron star (BNS) mergers via the the GW170817 event (The LIGO Scientific Collaboration & The Virgo Collaboration 2017), and the use of numerical simulations, it has become possible to establish a number of constraints on the equation of state (EOS) of nuclear matter (see, e.g., Bauswein et al. 2017; Margalit & Metzger 2017; Shibata et al. 2017; Malik et al. 2018; Radice et al. 2018; Raithel et al. 2018; Rezzolla et al. 2018; Ruiz et al. 2018; Tews et al. 2018; Montaña et al. 2019). Due to the degeneracy between tidal and stellar spin effects on the inspiral waveform, low- or high-spin priors are needed to infer the properties of the binaries from the gravitational-wave measurements (The LIGO Scientific Collaboration & The Virgo Collaboration 2017). Strong emphasis has been given to the low-spin priors under the expectation that the neutron stars (NSs) lose a significant fraction of their spin angular momentum through electromagnetic dipolar radiation well before the merger. While these assumptions favor irrotational NSs in the late inspiral and merger of BNSs, the parameter estimations from the gravitational-wave detections still strongly depend on the given a priori distribution of expected spins, with the high-spin prior leading to large uncertainties in the mass ratio and effective spin of the binary (Abbott et al. 2020).

Much of the theoretical modeling of BNS mergers has been concentrated on mass ratios $q := M_2/M_1 \gtrsim 0.7$ and on irrotational constituents (see, e.g., Shibata & Taniguchi 2006; Rezzolla et al. 2010; Bauswein et al. 2013; Dietrich et al. 2015; Lehner et al. 2016; Radice et al. 2016), in accordance with the (limited) sample of observed binary pulsar systems. However, the modeling of smaller ratios $q \gtrsim 0.45$ (Dietrich et al. 2017b; Most et al. 2021; Papenfort et al. 2021) and of higher spins has also started (Kastaun et al. 2013; Bernuzzi et al. 2014; East et al. 2016; Dietrich et al. 2017a; Most et al. 2019c). Given its impact on the electromagnetic counterpart, a particularly important prediction of the theoretical modeling has been the determination of whether the BNS underwent a prompt collapse at merger. The threshold mass discerning a prompt from a delayed collapse has been investigated thoroughly for irrotational binaries (see Baiotti & Rezzolla 2017; Burns 2020 for some reviews) using a number of EOSs. The natural expectation that M_{th} can be parameterized in terms of the maximum mass of a nonrotating NS, M_{TOV} (Bauswein et al. 2013), has been refined by more advanced parameterizations (Agathos et al. 2020; Koeppel et al. 2019) and by incorporating the effect of asymmetric binary systems (Bauswein et al. 2021). The latter resulted in a lowering of M_{th} at small mass ratios, i.e., $q \gtrsim 0.6$, depending on the stiffness of the EOS (Bauswein et al. 2021). Furthermore, simulations have suggested that the lifetime of merger remnants increases with the binary spin (Kastaun et al. 2013; Bernuzzi et al. 2014; East et al. 2016; Kiuchi et al. 2019), and decreases significantly at very small mass ratios (Rezzolla et al. 2010; Dietrich et al. 2017a; Kiuchi et al. 2019; Bernuzzi et al. 2020).
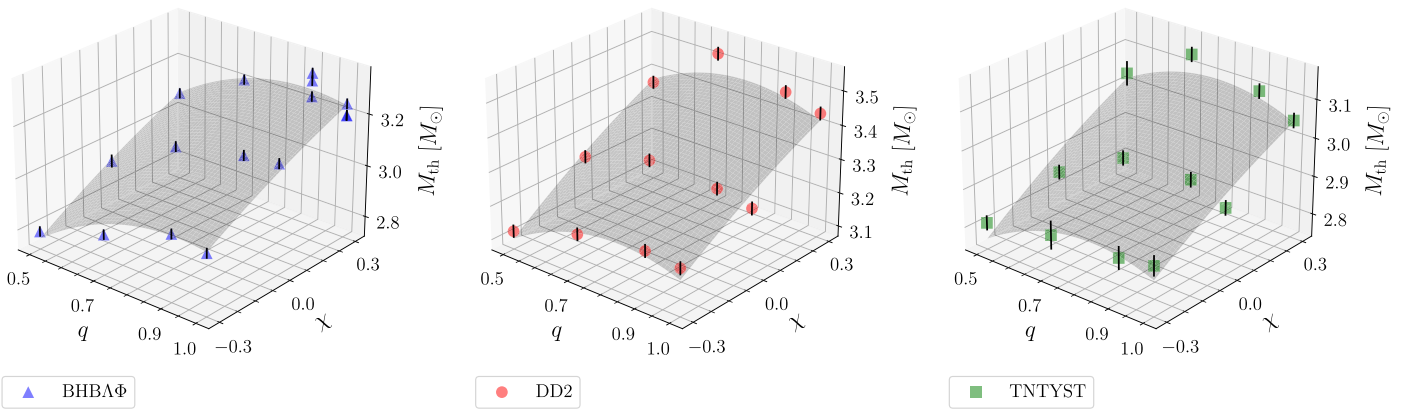
Figure 1. Dependence of M_{th} on the mass ratio and total spin of the binary. The three panels depict the data for the EOSs considered here, while the gray shaded surface represents the fit via the quadratic ansatz (3).

Using three temperature-dependent EOSs compatible with present astronomical observations, we report on a systematic exploration the effects that spin and mass asymmetry have on M_{th} of BNS configurations with a mass ratio in the range $0.5 \leqslant q \leqslant 1$, concentrating mostly on configurations in which the primary is spinning, while the secondary is irrotational. The large amount of data collected in this way has allowed us to derive a quasi-universal relation for M_{th} in terms of the mass ratio and spin of the binary.

2. Numerical Methods and Initial Data

Numerical methods. A significant hurdle to exploring asymmetric spinning binaries is the construction of initial data (ID) consistent with the Einstein equations. Here, we have used FUKA (Papenfort et al. 2021), the first publicly available ID solver able to reliably explore the needed parameter space. See Appendix A for details on the configurations considered. The evolution of the ID is performed using the Einstein Toolkit infrastructure that includes a fixed-mesh box-in-box refinement framework, Carpet (Schnetter et al. 2004). The spacetime evolution was handled by Antelope (Most et al. 2019b) using a constraint damping formulation of the Z4 system (Bernuzzi & Hilditch 2010; Alic et al. 2012). Finally, the general relativistic magnetohydrodynamic code, FIL (Most et al. 2019b), was used to evolve the fluid quantities. FIL is a derivative of the original IllinoisGRMHD code (Etienne et al. 2015) with the addition of high-order (fourth) conservative finite-differencing methods (Del Zanna et al. 2007). Importantly, FIL handles EOSs that are dependent on temperature and electron fraction, and includes a neutrino leakage scheme to handle neutrino cooling and weak interactions. The simulations were performed using a grid setup with an extent of ≈ 3000 km, decomposed in six levels of refinement, with the finest grid spacing being $\Delta x \approx 295$ m. For comparison, 36 simulations of higher resolution were performed with a finer grid spacing of $\Delta x \approx 221$ m, resulting in a measure of the error budget of $\sim 1\%$ ($\Delta M_{th} \simeq 0.03 \, M_\odot$).

Space of parameters. Pulsar observations have provided a wealth of information on the various rotation states that NSs can have including isolated pulsars with extreme spins and binary configurations with moderate to high spins. In general, most of the spin angular momentum of the binary is associated with the most massive of the two NSs, i.e., the primary (Lazarus et al. 2016). Hence, the spin configurations considered here are mostly centered on the effects χ_1 has on M_{th}. Here, 36

out of the 40 binaries considered have $\chi_1 = [-0.3, 0, 0.3]$ and $\chi_2 = 0$ where $\chi_{1,2} := J_{1,2}/M_{1,2}^2$ are, respectively, the dimensionless spins of the primary and secondary with spin angular momenta $J_{1,2}$. However, in order to gauge the impact of the spin of the secondary we also have considered four binary configurations with the same effective dimensionless spin $\tilde{\chi} := (1 + q)^{-1} (\chi_1 + q \chi_2)$.

Collapse-time measurement. A crucial aspect of any study wishing to determine M_{th} is a rigorous, systematic, and reproducible definition of what constitutes a collapse. Such an approach was previously not always considered, and very qualitative definitions of the threshold mass have been employed in the literature. Here, instead, we follow the prescription proposed by Koeppel et al. (2019), which tracks the minimum of the lapse to compute the collapse time and compares it to the shortest possible over which a prompt collapse can take place, that is, the freefall timescale. This approach, whose details can be found in Appendix B, allows not only for a precise definition and measurements, but also for the reproducibility of the results presented here.

3. Results

Dependence on mass ratio and spin. While the work of Koeppel et al. (2019) provided a first well-defined and rigorous manner of determining a quasi-universal relation for M_{th}, it was restricted to the analysis of equal mass, i.e., with $q = 1$ and irrotational binaries, i.e., with $\chi_1 = 0 = \chi_2$. In this specific scenario, M_{th} was found to depend on the EOS rather simply, so that a quasi-universal relation $M_{th} = M_{th}(\text{EOS})$ was proposed. However, it is clear that when considering the additional influence of spin and mass asymmetry, the functional dependence of M_{th} must account also for these additional degrees of freedom so that $M_{th} = M_{th}(\text{EOS}, q, \chi)$, where $\chi := \chi_1 + \chi_2$ is the total dimensionless spin of the binary.

Determining the *exact* expression for $M_{th}(\text{EOS}, q, \chi)$ clearly requires the exploration of the space of parameters in mass ratio and spin for any given EOS. As an example, we report in Figure 1 the dependence on the total spin and mass ratio of M_{th} for the three EOSs considered here. More specifically, shown with different colored symbols are the values of M_{th}—and the corresponding error bars, which are shown in black—as determined following the prescription discussed in Section 2 and by Koeppel et al. (2019) (see also Appendix B for an alternative approach leading to the same results), while the gray

shaded surfaces represent the best-fitting function to the data. Note that the fits for the three EOSs have variable errors, but all with a small chi-squared of $X^2_{\mathrm{BHB}\Lambda\Phi} = 0.001$, $X^2_{\mathrm{DD2}} = 0.001$, and $X^2_{\mathrm{TNTYST}} = 0.003$, all of which have an average (maximum) deviation from the fit that is 1% (2%). When expressed in absolute terms, the average deviations from the fits amount to $\Delta M_{\mathrm{th}} = 0.03\, M_{\odot}$.

Quasi-universal behavior. As can be readily appreciated from the inspection of Figure 1—which corresponds to 40 distinct binary configurations differing in mass ratio and spin—M_{th} shows a behavior that is similar for the three EOSs, but also that it leads to systematically different values for each of the EOSs considered. Determining accurately the threshold mass for each configuration has required the calculation of the inspiral and merger of about a dozen simulations with varying initial mass; the computational cost associated with Figure 1 is of about 360 simulations. Extending this work to an arbitrarily large number of EOSs is computationally prohibitive.

However, we can exploit the existence of a quasi-universal behavior of M_{th} (Bauswein et al. 2013; Agathos et al. 2020; Koeppel et al. 2019; Bauswein et al. 2021). More specifically, we extend the quasi-universal relation derived by Koeppel et al. (2019) by proposing that the functional dependence of $M_{\mathrm{th}}(\mathrm{EOS}, q, \chi)$ can be split into a part that is dependent on the EOS and a part dependent on q and χ. From a mathematical point of view, this essentially amounts to the separability in the functional dependence and hence in adopting the following ansatz:

$$M_{\mathrm{th}}(\mathrm{EOS}, q, \chi) = \kappa(\mathrm{EOS})f(q, \chi), \qquad (1)$$

where the dependence on the EOS is expressed via a multiplicative function following the study of Koeppel et al. (2019):

$$\kappa(\mathrm{EOS}) := \left(a - \frac{b}{1 - c\,\mathcal{C}_{\mathrm{TOV}}}\right)M_{\mathrm{TOV}}. \qquad (2)$$

where $\mathcal{C}_{\mathrm{TOV}}$ is the compactness of the nonrotating stellar configuration with the maximum mass and R_{TOV} its radius, i.e., $\mathcal{C}_{\mathrm{TOV}} := M_{\mathrm{TOV}}/R_{\mathrm{TOV}}$. The coefficients in Equation (2) have been reported by Koeppel et al. (2019) and are $a = 2b/(2-c)$, $b = 1.01$, and $c = 1.34$.

In practice, Equation (1) proposes that $f(q, \chi)$ is a surface that models M_{th} as a function of q and χ independently of the EOS. This surface can then be rescaled via a function describing the EOS, $\kappa(\mathrm{EOS}) = \kappa(R_{\mathrm{TOV}}, M_{\mathrm{TOV}})$, depending uniquely on the stellar compactness for the maximum-mass nonrotating configuration. Stated differently, the quasi-universal expression for M_{th} is expressed as $\hat{M}_{\mathrm{th}} := M_{\mathrm{th}}/\kappa(\mathrm{EOS})$, where all the dependence on the mass ratio and spin of the binary is contained in the function $f(q, \chi)$, whose behavior remains to be determined.

Considering the nonlinear behavior shown by the three fitting functions in Figure 1, it is natural to express the ansatz for $f(q, \chi)$ via a second-order polynomial, i.e.,

$$f(q, \chi) := a_1 + a_2(1 - q) + a_3\chi + a_4(1 - q)\chi$$
$$+ a_5(1 - q)^2 + a_6\chi^2. \qquad (3)$$

Since we wish to recover the quasi-universal fit obtained by Koeppel et al. (2019), we set $a_1 = 1$ in (3).

Note that the data clearly show a nonmonotonic growth of M_{th} as the mass asymmetry in the binary changes, which has
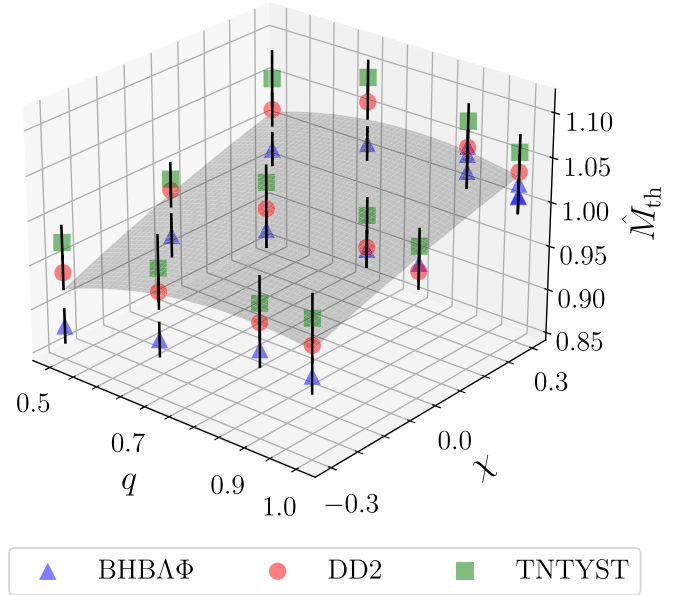
Figure 2. Similar to Figure 1, but highlighting the quasi-universal dependence of $\hat{M}_{\mathrm{th}}$ on the mass ratio and spin of the binary. Shown with different symbols are the values of $\hat{M}_{\mathrm{th}}$ and the corresponding uncertainties, while the gray shaded surface represents the fit via Equation (1).

been discussed already by East et al. (2016) and Bauswein et al. (2021) and more recently by Papenfort et al. (2021). Although the earlier works were restricted to nonspinning binaries with larger mass ratios, the evidence for a nonmonotonic dependence remained tentative and, indeed, the fitting expressions proposed by Bauswein et al. (2021) are monotonic. However, Papenfort et al. (2021) have shown nonmonotonic behavior should be expected due to an increase in accretion disk mass.

On the other hand, the presence of additional angular momentum in the system stabilizes the remnant against gravitational collapse (Breu & Rezzolla 2016; Weih et al. 2018). This implies that the fitting function f should monotonically increase with spin. Since the maximum dimensionless spin of uniformly rotating NSs is well constrained to be $\chi_{\mathrm{max}} \simeq 2 \times 0.65$ (see, e.g., the discussion in Most et al. 2020), we can improve (3) by requiring that M_{th} has a maximum for the maximum allowed value of the dimensionless spin, i.e.,

$$\partial_\chi f(q, \chi)|_{\chi_{\mathrm{max}}} = 0. \qquad (4)$$

Imposing (4) on (3) leads to

$$a_6 := -\frac{a_3 + a_4(1 - q)}{2\,\chi_{\mathrm{max}}}, \qquad (5)$$

thus leaving only four independent fitting coefficients, whose values are $a_2 = 0.11$, $a_3 = 0.12$, $a_4 = 0.07$, and $a_5 = -0.3$. We note that we obtain essentially the same coefficients either when fitting all the values of $\hat{M}_{\mathrm{th}}$ for the same values of q and χ or when averaging the coefficients obtained from the three distinct fits to the different EOSs (see Table 3 in Appendix A for the coefficients of the three fits).

Figure 2 reports the fit of the quasi-universal threshold mass for the combined data, showing an accurate representation of the functional behavior. Indeed, the fit yields a chi-squared of $X^2 = 0.028$, with an average (maximum) deviation from the fit of only $\sim 2\%$ ($\sim 6\%$). The very good match between the data
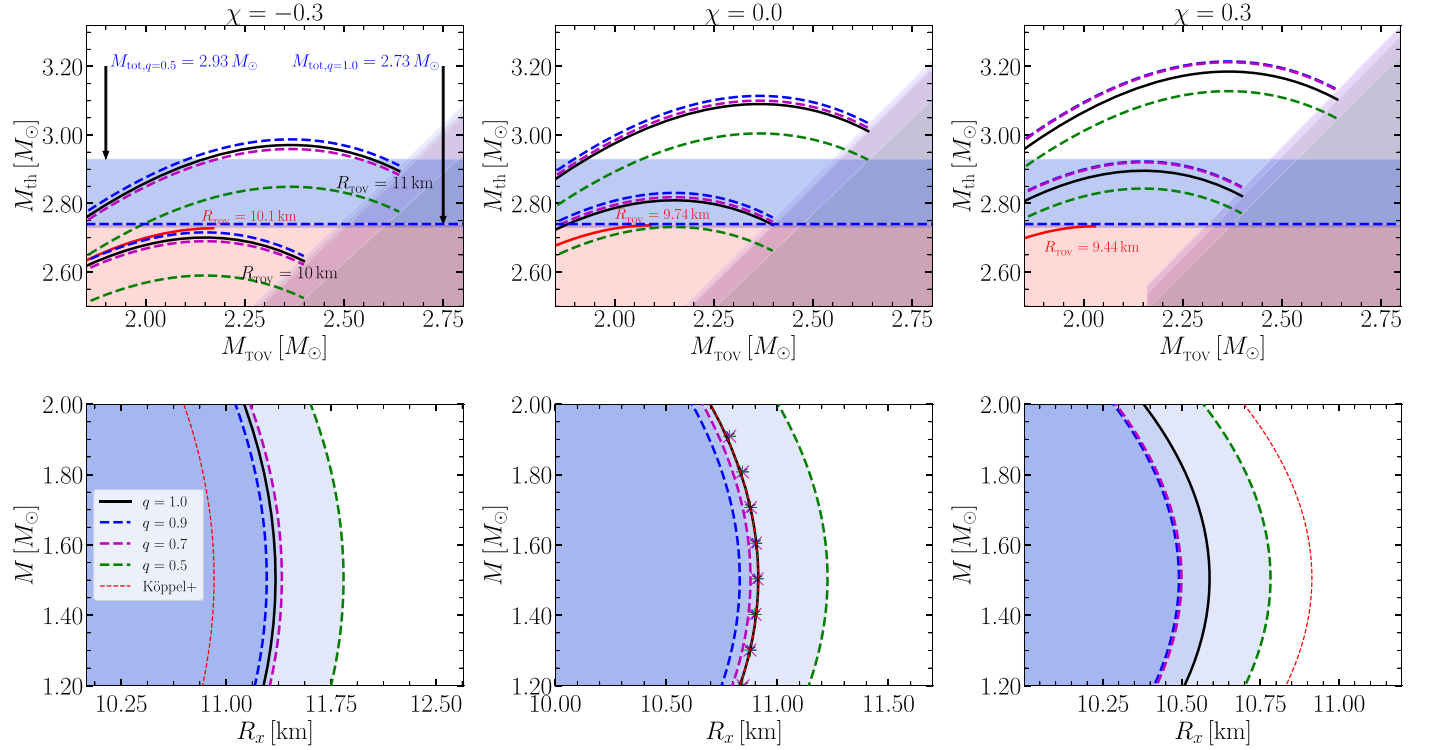
Figure 3. Top: the lower bounds on $R_{\mathrm{TOV},q=1}$ (red) using ansatz (1) for $R_{\mathrm{TOV}} = 10,\ 11$ km. The black continuous line corresponds to $q = 1$, while the colored dashed lines mark the constraints set by $q = 0.9,\ 0.7$, and 0.5. The blue region defines the mass of GW170817 and its uncertainty depending on q. The red shaded area shows the values excluded by the detection. The gray shaded area represents values excluded by the causality constraint. Each panel, from left to right, corresponds to $\chi = [-0.3, 0, 0.3]$, respectively. Bottom: universal relation for the lower limit of $R_x(M, q, \chi_1)$. In the middle panel, we demonstrate $R_x(M)$ is recovered when plotting $f(q, \chi)R_x(M, q, \chi)$. Overall, the top and bottom panels extend Figure 4 of Koeppel et al. (2019) to binaries with unequal masses and nonzero spin.

and the fitting function provides strong evidence for the existence of the quasi-universal behavior conjectured with the separability ansatz (1) and captures nicely the dependence of M_{th} on the mass ratio and spin of the binary. In particular, it highlights that—when compared to the irrotational case—M_{th} increases $\sim 6\%$ for the aligned-spin binaries considered here, and decreases $\sim 10\%$ for the antialigned spin binaries. We note that while the fit has considered all of the 40 binary configurations, we have verified that predictions for M_{th} made when considering only $\chi_2 = 0$ match equally well the numerical results obtained when χ_2 is nonzero.

Lower limits on the stellar radii. Following Koeppel et al. (2019), we can use Equations (1)—(3), to set lower limits on the radii of possible stellar models by computing sequences of M_{th} and M_{TOV} for fixed radii, as shown in Figure 3. More specifically, we recall that once a value for R_{TOV} is fixed, Equation (1) selects a line in the $(M_{\mathrm{th}}, M_{\mathrm{TOV}})$ plane. The first intersection of this line with the measured mass of a BNS with total mass M_{tot} that has not collapsed promptly sets a lower limit on M_{th} (Bauswein et al. 2017). This is shown in the upper panels of Figure 3 (see the left panel of Figure 4 of Koeppel et al. 2019)—one for each of the spins considered here—and where we report with a horizontal blue dashed line the total gravitational mass estimated for GW170817, $M_{\mathrm{tot},q=1} = 2.74^{+0.04}_{-0.01}\,M_\odot$ (The LIGO Scientific Collaboration & The Virgo Collaboration 2017). Since the mass ratio is not well known, the constraint for GW170817 is actually given by a band (blue shaded area) whose vertical edges depend on the mass ratio q (see arrows in the top left panel of Figure 3). Also reported in the top panels of Figure 3 with a gray shaded area is the limit set by causality and that requires $M_{\mathrm{TOV}}/R_{\mathrm{TOV}} \lesssim 0.354$.

In essence, therefore, the blue band constrains the red shaded area from above, yielding a lower limit for the radius of the maximum-mass star, $R_{\mathrm{TOV},q=1}$ (red solid line). The most important difference with a similar figure presented by Koeppel et al. (2019) for $q = 1$ and $\chi = 0$ is that we can now exploit the dependence of M_{th} on the mass ratio (and spin) to report the lower limit on R_{TOV} for different values of q (dashed lines). In this way it is possible to appreciate that in the case of antialigned spins (e.g., for $\chi = -0.3$), very strong constraints can be put on $R_{\mathrm{TOV},q=1}$ as the threshold mass is, in this case, considerably smaller (cf. $R_{\mathrm{TOV},q=1} = 10.24$ km for $\chi = -0.3$ versus $R_{\mathrm{TOV},q=1} = 9.44$ km for $\chi = 0.3$). Overall, the top panels in Figure 3 highlight how the knowledge of the mass ratio and spin of the binary can be extremely powerful in setting lower limits on the stellar radii.

As in the analysis by Koeppel et al. (2019), we can set lower limits not only for R_{TOV}, but for any arbitrary mass M. More specifically, we have found a fit for the minimum radius as a function of the mass ratio and spin in the binary, i.e., $R_x(M, q, \chi)$, and verified that this function can be recovered by the original expression $R_x(M)$ in Koeppel et al. (2019) for $q = 1$ and $\chi = 0$ (see symbols in the bottom middle panel of Figure 3):

$$R_x(M) = -0.88\,M^2 + 2.66\,M + 8.91, \qquad (6)$$

via the same scaling function $f(q, \chi)$ in Equation (3), namely,

$$R_x(M, q, \chi) = \frac{R_x(M)}{f(q, \chi)}. \qquad (7)$$

Because Equation (7) should be seen as an ansatz representative of the EOSs used here, it might need additional corrections

for EOSs that include strong phase transitions (Most et al. 2019a; Bauswein et al. 2020; Weih et al. 2020), or that include regimes of extremely high densities (Most & Raithel 2021).

The bottom panels of Figure 3 (see the right panel of Figure 4 of Koeppel et al. 2019) report the estimates of $R_x(M, q, \chi)$ for different values of q (different dashed lines) and χ (different columns); in each plot, we include the original fit for R_x from Koeppel et al. (2019) as a reference (red dashed line). Note that, for a given spin of the binary, the knowledge of the mass ratio can considerably increase the lower limit on the stellar radii, especially for systems with negative total spin. At the same time, given the nonmonotonic nature of the dependence on q, equal-mass systems do not necessarily yield the weakest constraint, which is instead attained for $q \simeq 0.8$–0.9.

4. Conclusions

We have performed the first systematic study of the impact that mass asymmetry and spin have on the threshold mass of BNS systems, M_{th}. We have done so by measuring M_{th} for 40 different BNS configurations encompassing three temperature-dependent EOSs, four mass ratios, and a systematic sampling of spin configurations. Using this data we have derived a quasi-universal relation for M_{th} and expressed its dependence on the mass ratio and spin of the binary. The new expression recovers the results of Koeppel et al. (2019) for equal-mass, irrotational binaries, and reveals that M_{th} can increase (decrease) by 5% (10%) for binaries that have spins aligned (antialigned) with the orbital angular momentum. In addition, we find evidence for a nonmonotonic dependence of M_{th} on the mass asymmetry in the system, which can be explained by an increase in accretion disk mass (Papenfort et al. 2021). Furthermore, we have extended to unequal masses and spinning binaries the lower limits that can be set on the stellar radii once a neutron star binary is detected, obtaining generic and analytic expressions for the minimum radii as a function of the mass ratio and of the total spin of the binary. In this way, we have highlighted that the merger of an unequal-mass, rapidly spinning binary can significantly constrain the allowed values of the stellar radii.

With more than 360 binaries simulated, this work has represented a challenge both for the associated computational costs and for the amount of data to be analyzed. Furthermore, while it has provided a first sparse but complete survey of the space of parameters to be expected in BNSs, it can be improved in a number of ways. First, by investigating more carefully the role played by spin of the secondary star. Second, by increasing the number of EOSs considered so—especially if they involve a softening from phase transitions (Most et al. 2019a; Weih et al. 2020)—as to further refine the properties of the quasi-universal behavior. Third, by elucidating the role played by the disruption of the stars at merger. Finally, by exploring the possibility that ultrastrong magnetic fields could modify the stability properties of the merged object and hence the threshold mass. We leave all of these improvements to future works.

Appendix A
Numerical Methods and Setup

Numerical simulations. As mentioned in the main text, our ID is constructed making use of the recently developed initial-data solver FUKA, which is based on the KADATH spectral solver library, solving the eXtended Conformal Thin Sandwich (XCTS) formulation of Einstein's field equations (Pfeiffer & York 2003, 2005; Papenfort et al. 2021). The ID are initially constructed using the force-balance equations to determine a quasi-circular orbit. The spin of each NS is achieved by modeling the velocity field of the fluid as a linear combination of a purely irrotational component and a uniformly rotating component (Tacik et al. 2015; Tsokaros et al. 2015; Papenfort et al. 2021). To minimize the eccentricity of the inspiral, we utilize 3.5 post-Newtonian (PN) order estimates of the expansion factor, $\dot{a}$, and the orbital velocity as discussed in Papenfort et al. (2021). This is important as quasi-circular ID for asymmetric binaries and binaries with spinning objects result in very eccentric inspirals that are also discussed in Papenfort et al. (2021). Additionally, it has been shown that eccentricity can have an impact on the stability of the remnant (East et al. 2016); therefore, the use of 3.5 PN estimates is important to obtain accurate measurements of M_{th}. Finally, the initial separations of the compact objects are set to 50 km, thus allowing the binary to equilibrate over the course of a few orbits prior to merger due to the approximations used in the initial-data construction.

Realistic, hot EOSs. The binaries simulated here have been modeled with three different realistic and temperature-dependent (hot) EOSs. In particular, they are the rather soft TNTYST EOS (Togashi et al. 2017), the rather stiff BHBΛΦ EOS (Banik et al. 2014), and the intermediate (HS-)DD2 EOS (Typel et al. 2010). The most salient properties of these EOSs, namely, the maximum mass of the nonrotating configuration, the corresponding radius, the compactness, and the freefall timescales are reported in Table 1.

Spin configurations. Emphasis in our analysis has been placed on low-spin priors and on the role of the spin of the primary in determining the threshold mass. Hence, the large majority of our binaries have an irrotational secondary (i.e., $\chi_2 = 0$). However, binaries with nonnegligible mixed spins cannot be ruled out; thus, we have performed additional spot tests that include configurations of constant mass ratio and

Table 1
For the EOSs Considered Here We Report the Maximum Mass of a Nonrotating Configuration, M_{TOV}, Together with the Corresponding Radius, R_{TOV}, Compactness, C_{TOV}, and Freefall Timescale τ_{TOV}

	M_{TOV} ($M_\odot$)	R_{TOV} (km)	C_{TOV}	τ_{TOV} (μs)
BHBΛΦ	2.10	11.64	0.26	83.31
DD2	2.42	11.94	0.30	80.60
TNTYST	2.23	10.17	0.32	66.12

Table 2
Lists of the Binary Configurations Explored in This Study for the Three Nuclear EOSs Considered

	M_{th} $(M_\odot)$	$\mathcal{M}_{\mathrm{th}}$ $(M_\odot)$	M_1 $(M_\odot)$	M_2 $(M_\odot)$	q	χ_1	χ_2	$\tilde{\chi}$	EOS
BHBΛΦ.1.0.−0.3	2.961	1.289	1.481	1.481	1.0	−0.3	0.0	−0.150	BHBΛΦ
BHBΛΦ.1.0.+0.0	3.149	1.370	1.574	1.574	1.0	0.0	0.0	0.000	BHBΛΦ
BHBΛΦ.1.0.+0.2	3.197	1.392	1.599	1.599	1.0	0.2	0.1	0.150	BHBΛΦ
BHBΛΦ.1.0.+0.3	3.199	1.392	1.600	1.600	1.0	0.3	0.0	0.150	BHBΛΦ
BHBΛΦ.1.0.+0.4	3.242	1.411	1.621	1.621	1.0	0.4	−0.1	0.150	BHBΛΦ
BHBΛΦ.0.9.−0.3	2.982	1.296	1.569	1.412	0.9	−0.3	0.0	−0.158	BHBΛΦ
BHBΛΦ.0.9.+0.0	3.134	1.362	1.649	1.484	0.9	0.0	0.0	0.000	BHBΛΦ
BHBΛΦ.0.9.+0.2	3.227	1.402	1.699	1.529	0.9	0.2	0.1	0.158	BHBΛΦ
BHBΛΦ.0.9.+0.3	3.288	1.429	1.731	1.558	0.9	0.3	0.0	0.158	BHBΛΦ
BHBΛΦ.0.9.+0.4	3.317	1.442	1.746	1.571	0.9	0.4	−0.1	0.158	BHBΛΦ
BHBΛΦ.0.7.−0.3	2.879	1.230	1.694	1.185	0.7	−0.3	0.0	−0.176	BHBΛΦ
BHBΛΦ.0.7.+0.0	3.077	1.314	1.810	1.267	0.7	0.0	0.0	0.000	BHBΛΦ
BHBΛΦ.0.7.+0.3	3.209	1.371	1.888	1.321	0.7	0.3	0.0	0.176	BHBΛΦ
BHBΛΦ.0.5.−0.3	2.791	1.132	1.861	0.930	0.5	−0.3	0.0	−0.200	BHBΛΦ
BHBΛΦ.0.5.+0.0	2.929	1.188	1.952	0.976	0.5	0.0	0.0	0.000	BHBΛΦ
BHBΛΦ.0.5.+0.3	3.071	1.246	2.048	1.024	0.5	0.3	0.0	0.200	BHBΛΦ
DD2.1.0.−0.3	3.209	1.397	1.605	1.605	1.0	−0.3	0.0	−0.150	DD2
DD2.1.0.+0.0	3.266	1.421	1.633	1.633	1.0	0.0	0.0	0.000	DD2
DD2.1.0.+0.3	3.437	1.496	1.718	1.718	1.0	0.3	0.0	0.150	DD2
DD2.0.9.−0.3	3.219	1.399	1.694	1.525	0.9	−0.3	0.0	−0.158	DD2
DD2.0.9.+0.0	3.287	1.428	1.730	1.557	0.9	0.0	0.0	0.000	DD2
DD2.0.9.+0.3	3.467	1.507	1.825	1.642	0.9	0.3	0.0	0.158	DD2
DD2.0.7.−0.3	3.190	1.362	1.877	1.314	0.7	−0.3	0.0	−0.176	DD2
DD2.0.7.+0.0	3.299	1.409	1.940	1.358	0.7	0.0	0.0	0.000	DD2
DD2.0.7.+0.3	3.517	1.502	2.069	1.448	0.7	0.3	0.0	0.176	DD2
DD2.0.5.−0.3	3.123	1.267	2.082	1.041	0.5	−0.3	0.0	−0.200	DD2
DD2.0.5.+0.0	3.240	1.314	2.160	1.080	0.5	0.0	0.0	0.000	DD2
DD2.0.5.+0.3	3.369	1.366	2.246	1.123	0.5	0.3	0.0	0.200	DD2
TNTYST.1.0.−0.3[*]	2.870	1.249	1.435	1.435	1.0	−0.3	0.0	−0.150	TNTYST
TNTYST.1.0.+0.0	2.916	1.269	1.458	1.458	1.0	0.0	0.0	0.000	TNTYST
TNTYST.1.0.+0.3	3.048	1.327	1.524	1.524	1.0	0.3	0.0	0.150	TNTYST
TNTYST.0.9.−0.3[*]	2.855	1.241	1.503	1.352	0.9	−0.3	0.0	−0.158	TNTYST
TNTYST.0.9.+0.0	2.956	1.284	1.556	1.400	0.9	0.0	0.0	0.000	TNTYST
TNTYST.0.9.+0.3	3.095	1.345	1.629	1.466	0.9	0.3	0.0	0.158	TNTYST
TNTYST.0.7.−0.3[*]	2.845	1.215	1.674	1.171	0.7	−0.3	0.0	−0.176	TNTYST
TNTYST.0.7.+0.0	2.950	1.260	1.735	1.214	0.7	0.0	0.0	0.000	TNTYST
TNTYST.0.7.+0.3	3.135	1.339	1.844	1.290	0.7	0.3	0.0	0.176	TNTYST
TNTYST.0.5.−0.3	2.810	1.139	1.873	0.936	0.5	−0.3	0.0	−0.200	TNTYST
TNTYST.0.5.+0.0	2.850	1.156	1.900	0.950	0.5	0.0	0.0	0.000	TNTYST
TNTYST.0.5.+0.3[*]	3.030	1.229	2.020	1.010	0.5	0.3	0.0	0.200	TNTYST

Note. Included is the determined threshold mass, M_{th}; the corresponding chirp mass, $\mathcal{M}_{\mathrm{th}}$; the ADM mass, M_{ADM}, of each NS at infinite separation; the dimensionless spin of the each NS, χ_1, χ_2; and the effective spin of the binary, $\tilde{\chi}$. In all cases, the spin axis is parallel to the orbital rotation axis. M_{th} in configurations with a [*] were obtained using the *averaging method* as discussed in the Appendix Materials.

effective spin, but with a spinning secondary so as to ascertain the difference in the collapse time using the BHBΛΦ EOS. All of the 40 binaries considered here and their properties are collected in Table 2.

With the data collected in this way we have performed a double analysis. First, we have considered only binaries with irrotational secondaries and performed the fits as discussed in the main text. Next, using the resulting coefficients we have compared the predictions of the fit with the actual numerical results of the four binaries with a spinning secondary. In this way, we have found that the analytic predictions and the numerical results differ by less than 3% and are therefore well within the average error of the fit. Overall, this result has given us confidence that the spin of the secondary has a negligible impact on M_{th}, which is instead dynamically dominated by the

spin of the primary. This is a reasonable estimate for two distinct reasons. First, M_{th} effectively measures the strength of the gravitational field of the merged object and is therefore dominated by the properties of the primary. Second, the modifications on M_{th} due to spin are, overall, not large. As a second approach, we have performed a fit using all of the data available and this is what is actually presented in the main text; the corresponding values of the fitting coefficients and their uncertainties are collected in Table 3.

Appendix B
Comparison of Threshold Mass Measurements

To determine M_{th} from our numerical simulations we have elected to utilize the method of measuring the collapse time, t_{col}, as proposed in Koeppel et al. (2019) given the physical

Table 3
Values of the Fitting Coefficients and Their Uncertainty in the Functional Ansatz (3) in the Main Text

FIT	a_1	a_2	a_3	a_4	a_5
BHBΛΦ	0.982 ± 0.005	0.08 ± 0.06	0.14 ± 0.02	0.04 ± 0.06	-0.4 ± 0.1
DD2	0.997 ± 0.007	0.13 ± 0.08	0.12 ± 0.02	0.04 ± 0.08	-0.3 ± 0.1
TNTYST	1.024 ± 0.008	0.14 ± 0.08	0.12 ± 0.03	0.04 ± 0.09	-0.3 ± 0.2
Univ	1	0.11 ± 0.07	0.12 ± 0.03	0.07 ± 0.09	-0.3 ± 0.2

Note. The first three rows refer to the specific EOSs considered here and the last one to the quasi-universal expression

motivation behind it. We will reference this as the *freefall* method, which is discussed below. However, similar measurements can be made with minimal impact to the result of the measured value of M_{th} by using a simpler approach, which we refer to as the *averaging* method, and which averages the masses of the two binaries closest to the critical value leading to a prompt collapse.

Freefall method. The original method of measuring the collapse time, t_{col}, as proposed in Koeppel et al. (2019), is defined by tracking the minimum of the lapse, $\tilde{\alpha} := \min(\alpha)$. While this approach is adequate for equal-mass, nonspinning binaries, it leads to potential biases when considering unequal-mass and spinning binaries, since the lapse is not only dependent on the length scales of the system, but it is strongly impacted by asymmetries in the system. Therefore, when performing measurements of the collapse time, t_{col}, we analyze $\tilde{\alpha}$ when normalized by its maximum, which we define as $\hat{\alpha} := \tilde{\alpha}/\max(\tilde{\alpha})$.

Because of this rescaling, new brackets must be applied to determine the time of merger, t_{merge}, and the time of black hole formation, t_{BH}. To do so, we set as the merger time the coordinate time such that

$$t_{merg}: \qquad \hat{\alpha}_{merge} = 0.9. \qquad (B1)$$

Similarly, we set as the threshold for black hole formation and the related coordinate time to be

$$t_{BH}: \qquad \hat{\alpha}_{BH} = 0.1, \qquad (B2)$$

such that the remnant is gravitationally unstable across all EOSs and configurations considered and the formation of a BH is certain. Note that the merged object never collapses faster than the shortest freefall timescale ($t_{col} >= \tau_{ff}$) where the freefall timescale is defined as (Rezzolla & Zanotti 2013)

$$\tau_{ff}(M, R) := \frac{\pi}{2}\sqrt{\frac{R^3}{2M}}, \qquad (B3)$$

and the shortest τ_{ff} occurs at $\tau_{TOV} := \tau_{ff}(M_{TOV}, R_{TOV})$ and is a physically well motivated lower limit. We recognize that both of these markers are somewhat arbitrary, but as done in Koeppel et al. (2019), they reproduce well the behavior of the binaries when other markers, e.g., the time of the maximum of the gravitational-wave emission and the time of the appearance of a black hole ringdown, are used.

Using these markers, we measure the collapse time as defined as

$$t_{col} := t_{BH} - t_{merg}, \qquad (B4)$$

which is the same as the prescription from Koeppel et al. (2019), but here it is calculated based on $\hat{\alpha}$ and with different bracket values. In Figure 4 we show examples of how $\hat{\alpha}$ versus
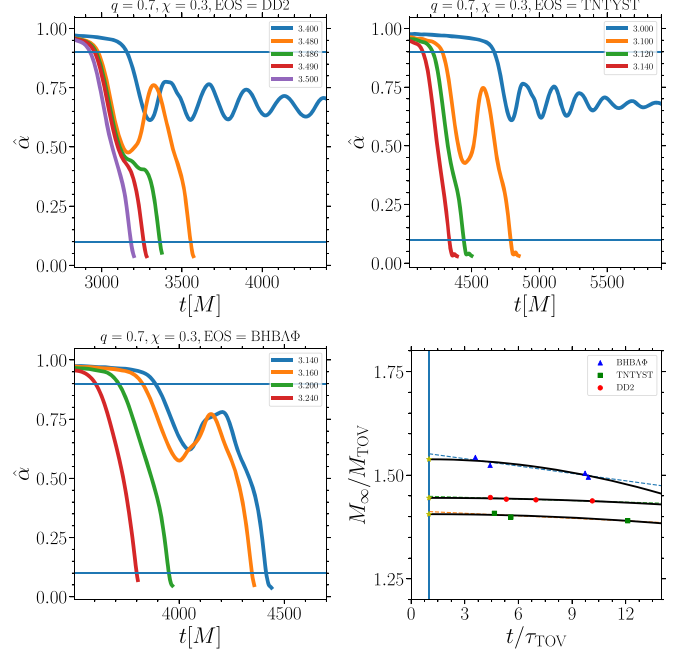
Figure 4. Top and bottom left: plots of normalized minimum lapse, $\hat{\alpha}$, for $q = 0.7$ and $\chi = 0.3$ for each of the EOSs used in this work. Horizontal lines mark the threshold values to define merger and black hole formation, i.e., $\hat{\alpha}_{merge} = 0.9$ and $\hat{\alpha}_{BH} = 0.1$, respectively. Bottom right: example of measuring M_{th} using the *freefall* method for the three EOSs; dashed lines denote a linear-fit result.

coordinate time looks for all equations with $q = 0.7$, $\chi_1 = 0.3$, $\chi_2 = 0$. Additionally, one panel shows the fit for the three EOSs and the extrapolation for $t/\tau_{TOV} \to 1$, as discussed by Koeppel et al. (2019).

Averaging method. As from its name, the *averaging* method simply averages the masses of the two binaries that are closest to the critical threshold mass, with M_{sup} being the *supercritical* value and M_{sub} the *subcritical* one, i.e.,

$$M_{th} := \frac{1}{2}(M_{sup} + M_{sub}). \qquad (B5)$$

To distinguish between the two cases, we define as supercritical any binary whose evolution of the normalized lapse sharply decreases to the lower limit $\hat{\alpha} = 0.1$ without a characteristic post-merger local maximum. On the other hand, we define as subcritical any binary whose evolution of the normalized lapse shows a local maximum after merger indicating, therefore, that the merged object has contracted but also expanded at least in one complete oscillation.

Obviously, the averaging method is far simpler (it does not require any fitting or extrapolation) but also does not provide any measure of how close M_{sup} and M_{sub} are from M_{th}.

Interestingly, we have measured $M_{\rm th}$ using the averaging method against the freefall method and obtained the same results with an average (maximum) difference relative to the value obtained using the freefall method of $<1\%$ ($\sim2\%$). The situations in which the averaging method is to be preferred is when the difference between $M_{\rm sup}$ and $M_{\rm sub}$ is $<1\%$, in which case the error in measuring $M_{\rm th}$ would be dominated by the evolution resolution. This was particularly useful in the case of the TNTYST EOS, where the separation between the supercritical and subcritical solutions was very small in some specific mass ratios and spins.

Both of the methods outlined require a definition on whether or a not a data set is supercritical or subcritical. In this work we use the definition such that $\hat{\alpha}|^{t_{\rm BH}}_{t_{\rm merg}}$ diverges directly. We note the use of the time derivative of $\hat{\alpha}$ is important especially in the highly asymmetric binaries as the collapse behavior is less apparent when only considering $\hat{\alpha}$.

ORCID iDs

Samuel D. Tootle ⓘ https://orcid.org/0000-0001-9781-0496
L. Jens Papenfort ⓘ https://orcid.org/0000-0002-6400-2553
Elias R. Most ⓘ https://orcid.org/0000-0002-0491-1210
Luciano Rezzolla ⓘ https://orcid.org/0000-0002-1330-7103

References

Abbott, B. P., Abbott, R., Abbott, T. D., et al. 2020, ApJL, 892, L3
Agathos, M., Zappa, F., Bernuzzi, S., et al. 2020, PhRvD, 101, 044006
Alic, D., Bona-Casas, C., Bona, C., Rezzolla, L., & Palenzuela, C. 2012, PhRvD, 85, 064040
Baiotti, L., & Rezzolla, L. 2017, RPPh, 80, 096901
Banik, S., Hempel, M., & Bandyopadhyay, D. 2014, ApJS, 214, 22
Bauswein, A., Baumgarte, T. W., & Janka, H.-T. 2013, PhRvL, 111, 131101
Bauswein, A., Blacker, S., Lioutas, G., et al. 2021, PhRvD, 103, 123004
Bauswein, A., Blacker, S., Vijayan, V., et al. 2020, PhRvL, 125, 141103
Bauswein, A., Just, O., Janka, H.-T., & Stergioulas, N. 2017, ApJL, 850, L34
Bernuzzi, S., Breschi, M., Daszuta, B., et al. 2020, MNRAS, 497, 1488
Bernuzzi, S., Dietrich, T., Tichy, W., & Brügmann, B. 2014, PhRvD, 89, 104021
Bernuzzi, S., & Hilditch, D. 2010, PhRvD, 81, 084003
Breu, C., & Rezzolla, L. 2016, MNRAS, 459, 646
Burns, E. 2020, LRR, 23, 4
Del Zanna, L., Zanotti, O., Bucciantini, N., & Londrillo, P. 2007, A&A, 473, 11
Dietrich, T., Bernuzzi, S., Ujevic, M., & Tichy, W. 2017a, PhRvD, 95, 044045
Dietrich, T., Moldenhauer, N., Johnson-McDaniel, N. K., et al. 2015, PhRvD, 92, 124007
Dietrich, T., Ujevic, M., Tichy, W., Bernuzzi, S., & Brügmann, B. 2017b, PhRvD, 95, 024029
East, W. E., Paschalidis, V., Pretorius, F., & Shapiro, S. L. 2016, PhRvD, 93, 024011
Etienne, Z. B., Paschalidis, V., Haas, R., Mösta, P., & Shapiro, S. L. 2015, CQGra, 32, 175009
Grandclement, P. 2010, JCoPh, 229, 3334
Kastaun, W., Galeazzi, F., Alic, D., Rezzolla, L., & Font, J. A. 2013, PhRvD, 88, 021501
Kiuchi, K., Kyutoku, K., Shibata, M., & Taniguchi, K. 2019, ApJ, 876, L31
Koeppel, S., Bovard, L., & Rezzolla, L. 2019, ApJL, 872, L16
Lazarus, P., Freire, P. C. C., Allen, B., et al. 2016, ApJ, 831, 150
Lehner, L., Liebling, S. L., Palenzuela, C., et al. 2016, CQGra, 33, 184002
Loeffler, F., Faber, J., Bentivegna, E., et al. 2012, CQGra, 29, 115001
Malik, T., Alam, N., Fortin, M., et al. 2018, PhRvC, 98, 035804
Margalit, B., & Metzger, B. D. 2017, ApJL, 850, L19
Montaña, G., Tolós, L., Hanauske, M., & Rezzolla, L. 2019, PhRvD, 99, 103009
Most, E. R., Papenfort, L. J., Dexheimer, V., et al. 2019a, PhRvL, 122, 061101
Most, E. R., Papenfort, L. J., & Rezzolla, L. 2019b, MNRAS, 490, 3588
Most, E. R., Papenfort, L. J., Tootle, S., & Rezzolla, L. 2021, ApJ, 912, 80
Most, E. R., Papenfort, L. J., Tsokaros, A., & Rezzolla, L. 2019c, ApJ, 884, 40
Most, E. R., Papenfort, L. J., Weih, L. R., & Rezzolla, L. 2020, MNRAS, 499, L82
Most, E. R., & Raithel, C. A. 2021, arXiv:2107.06804
Papenfort, L. J., Tootle, S. D., Grandclément, P., Most, E. R., & Rezzolla, L. 2021, PhRvD, 104, 024057
Papenfort, L. J., Tootle, S. D., Most, E. R., & Rezzolla, L. 2021, MNRAS, submitted
Pfeiffer, H. P., & York, J. W. 2003, PhRvD, 67, 044022
Pfeiffer, H. P., & York, J. W. 2005, PhRvL, 95, 091101
Radice, D., Galeazzi, F., Lippuner, J., et al. 2016, MNRAS, 460, 3255
Radice, D., Perego, A., Zappa, F., & Bernuzzi, S. 2018, ApJL, 852, L29
Raithel, C., Özel, F., & Psaltis, D. 2018, ApJ, 857, L23
Rezzolla, L., Baiotti, L., Giacomazzo, B., Link, D., & Font, J. A. 2010, CQGra, 27, 114105
Rezzolla, L., Most, E. R., & Weih, L. R. 2018, ApJL, 852, L25
Rezzolla, L., & Zanotti, O. 2013, Relativistic Hydrodynamics (Oxford: Oxford Univ. Press)
Ruiz, M., Shapiro, S. L., & Tsokaros, A. 2018, PhRvD, 97, 021501
Schnetter, E., Hawley, S. H., & Hawke, I. 2004, CQGra, 21, 1465
Shibata, M., Fujibayashi, S., Hotokezaka, K., et al. 2017, PhRvD, 96, 123012
Shibata, M., & Taniguchi, K. 2006, PhRvD, 73, 064027
Tacik, N., Foucart, F., Pfeiffer, H. P., et al. 2015, PhRvD, 92, 124012
Tews, I., Margueron, J., & Reddy, S. 2018, PhRvC, 98, 045804
The LIGO Scientific CollaborationThe Virgo Collaboration 2017, PhRvL, 119, 161101
Togashi, H., Nakazato, K., Takehara, Y., et al. 2017, NucPh, A961, 78
Tsokaros, A., Uryū, K., & Rezzolla, L. 2015, PhRvD, 91, 104030
Typel, S., Röpke, G., Klähn, T., Blaschke, D., & Wolter, H. H. 2010, PhRvC, 81, 015803
Weih, L. R., Hanauske, M., & Rezzolla, L. 2020, PhRvL, 124, 171103
Weih, L. R., Most, E. R., & Rezzolla, L. 2018, MNRAS, 473, L126